Applied Surface Science 282 (2013) 789–797

Contents lists available at SciVerse ScienceDirect

Applied Surface Science

journal homepage: www.elsevier.com/locate/apsusc

Structural morphology and characterization of (AlCrMoTaTi)N coating deposited via magnetron sputtering

Du-Cheng Tsai [a], Zue-Chin Chang [b], Bing-Hau Kuo [a], Ming-Hua Shiao [c], Shou-Yi Chang [a], Fuh-Sheng Shieu [a,*]

[a] Department of Materials Science and Engineering, National Chung Hsing University, Taichung 40227, Taiwan
[b] Department of Mechanical Engineering, National Chin-Yi University of Technology, Taichung 41170, Taiwan
[c] Instrument Technology Research Center, National Applied Research Laboratories, Hsinchu 300, Taiwan

ARTICLE INFO

Article history:
Received 8 February 2013
Received in revised form 31 May 2013
Accepted 2 June 2013
Available online 18 June 2013

Keywords:
Coating materials
Nitride materials
Vapor deposition
Crystal structure
Transmission electron microscopy (TEM)

ABSTRACT

(AlCrMoTaTi)N coatings were deposited on Si substrates via reactive magnetron sputtering. The effects of N_2-to-total (N_2 + Ar) flow ratio (R_N) on the coating structure and properties were examined. Alloy coatings have composite equiaxed grain structures consisting of amorphous and body-centered cubic crystal phases, whereas nitride coatings have columnar structures with single face-centered cubic crystal phase. Distinct lattice expansion and grain refinement were observed in nitride coatings as R_N increased. Typical V-shaped columnar structures with faceted tops and open column boundaries transformed into denser and smaller columnar structures with domed surfaces. Increasing R_N to 30% caused the hardness and modulus to reach maximum values of 30.6 and 291.6 GPa, respectively. Electrical resistivity increased from 536 μΩ cm to 8212 μΩ cm when R_N increased from 10% to 50%.

1. Introduction

Transition metal nitride coatings have been widely used as protective surface coatings for molding and cutting tools since the 1970s [1]. The service lives of these tools are significantly prolonged and their commercial values increase because of their functional properties such as high hardness, high melting point, and excellent chemical and oxidation resistances. These properties are strongly affected by material composition and preparation conditions. Metal nitride coatings with enhanced properties have been synthesized using various deposition techniques and conditions. These coatings exhibit the widest variety of microstructures among materials in terms of grain size, crystallographic orientation, lattice defects, texture, surface morphology, and phase composition. However, the demand for high performance requires the addition of different elements to existing nitrides to modify their properties for specific applications. Ternary Ti–Al–N [2,3] and Ti–Si–N [4,5] systems with higher hardness values and oxidation resistances compared with their TiN binary counterparts were developed. Alloying nitride coatings with appropriate elements can effectively modify the coating properties.

High-entropy alloys (HEA), comprising at least five principal metal elements in near-equimolar ratios, have recently gained much attention for their potential use in various applications [6,7]. These alloys possess simple solid solution structures and versatile properties caused by high mixing entropy and lattice distortion effects. Based on similar concepts, metallic, nitride, and oxide coatings derived from HEA targets are also investigated intensively and shown to have great potential in coating applications. In these studies, TiVCrZrY, TiVCrZrHf, and AlCrTaTiZr nitrides exhibit hardness values ranging from 17 GPa to 32 GPa when deposited without substrate biases or heating [8–10]. Their hardness can be further improved to 36 GPa up to 48 GPa under biased or heated conditions [11–13].

At present, developments in advanced hard coatings with enhanced performances use more elements to form solid solution structures or even nanocomposite structures with at least two constituent phases. Among binary nitride coatings, TiN, CrN, and TaN have attracted considerable attention because of their satisfactory mechanical properties [1,14–16]. Adding Al into cubic nitride structures not only enhances thermal properties, but also increases hardness. The former is due to the formation of a protective Al-rich oxide layer on the coating surface, whereas the latter is attributed to a solid-solution strengthening effect. MoN incorporation provides low friction coefficients as a result of the solid state lubricious properties of molybdenum trioxides [17]. Therefore, in this study, (AlCrMoTaTi)N coatings were deposited

* Corresponding author. Tel.: +886 4 2284 0500; fax: +886 4 2285 7017.
E-mail address: fsshieu@dragon.nchu.edu.tw (F.-S. Shieu).

0169-4332/$ – see front matter © 2013 Elsevier B.V. All rights reserved.
http://dx.doi.org/10.1016/j.apsusc.2013.06.057

via reactive radio-frequency (RF) magnetron sputtering using AlCrMoTaTi targets. The effects of N_2-to-total (N_2 + Ar) flow ratio (R_N) on the microstructure and properties of deposited coatings were examined.

2. Experimental

(AlCrMoTaTi)N coatings were deposited onto p-Si (1 0 0) wafers using an RF magnetron sputtering system with equimolar AlCrMoTaTi targets 50 mm in diameter. The target alloy was fabricated by conventional powder metallurgy technology. Before deposition, the Si substrates were cleaned, and then rinsed with ethanol and distilled water in an ultrasonic bath. The (AlCrMoTaTi)N coatings were deposited at room temperature in an Ar + N_2 atmosphere under an RF power of 150 W and a working pressure of 6×10^{-3} Torr. The bias of the substrate was fixed at −100 V. During deposition, the total gas flow-rate ratio was maintained at 30 sccm, and R_N was varied from 0% to 50%. Deposition time was increased with an increase in R_N to maintain the coating thickness at approximately 1 μm. Targets were presputtered with Ar to remove their surface oxide layers before deposition.

The chemical compositions of the coatings were determined using a JEOL JXA-8800M field-emission electron probe microanalyzer. At least three tests were performed for each sample. The crystal structures were analyzed using a grazing-incidence (1°) BRUKER D8 Discover X-ray diffractometer using Cu Kα radiation at a scanning speed of 1°/min. From the full width at half maximum intensity, the average grain sizes of the coatings were calculated using the Scherrer formula [18]. Morphological studies and thickness measurements were performed using a JEOL JSM-6700F field-emission scanning electron microscope (SEM). The deposition rate was obtained by dividing the thickness with the deposition time. Microstructural examinations were conducted using an FEI E.O. Tecnai F20 transmission electron microscope (TEM). The surface roughness (root-mean-square) values of the coatings were derived using a Seiko SPA400 atomic force microscope (AFM). Hardness values and elastic moduli of the coatings were measured using a TriboLab nanoindenter. At least five tests were performed for each sample. Electrical resistivities of the coatings were measured using a four-point probe system.

3. Results and discussion

3.1. Chemical composition and deposition rate

Fig. 1 shows the EPMA chemical analysis element concentrations in the (AlCrMoTaTi)N coatings deposited at various R_N values. For AlCrMoTaTi alloy coatings, the ratio of the target elements in the coatings deviates significantly from the ratio in the targets. This difference was due to the different atomic weights and sputtering yields among the target elements. Accordingly, the reduced Al, Cr, and Ti concentrations in the resultant coating are attributed to their lower atomic weights, causing these atoms to scatter more easily during flight before deposition. The higher Cr concentration compared with that of Ti may have been caused by the higher Cr sputtering yield [19]. Introducing nitrogen resulted in variations in the representation of target elements in the product coating probably because of the strong affinity for target elements and nitrogen. As R_N reached 10%, the nitrogen content increased sharply to 37.5 at.% and approached 51 at.% at R_N = 50%. These coatings can be regarded as nitride coatings. The effect of R_N on the deposition rate is shown in Fig. 2, indicating that the deposition rate initially increases from R_N = 0% to 10%, then gradually decreases with further increase in R_N. The initial deposition rate increase may be attributed to the incorporation of nitrogen or the formation of loose structures,

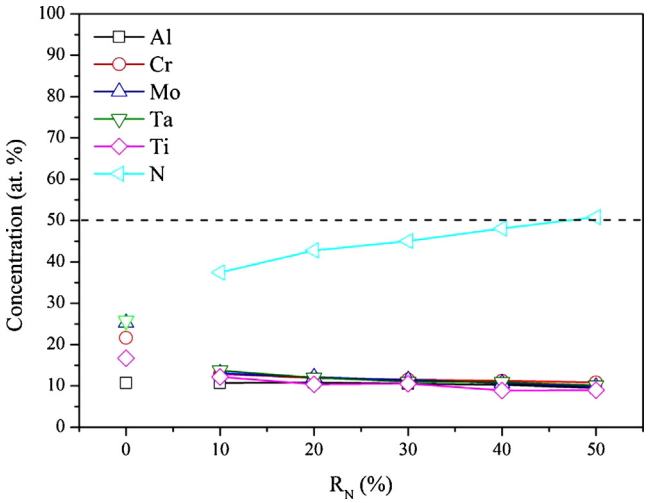

Fig. 1. EPMA element contents in (AlCrMoTaTi)N coatings deposited at various R_N.

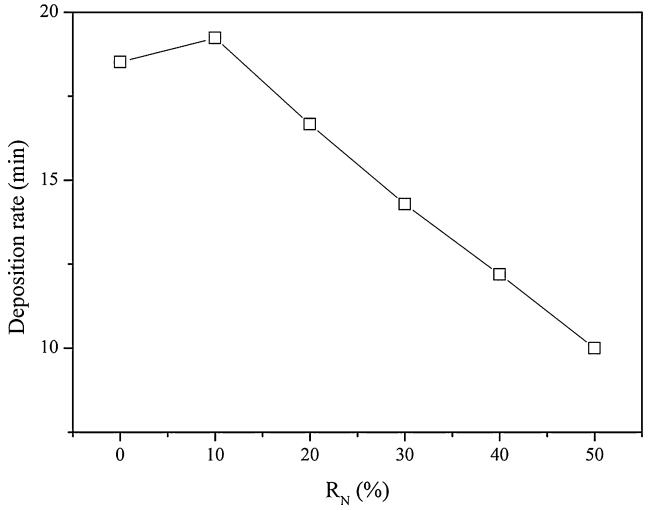

Fig. 2. Deposition rate of (AlCrMoTaTi)N coatings deposited at various R_N.

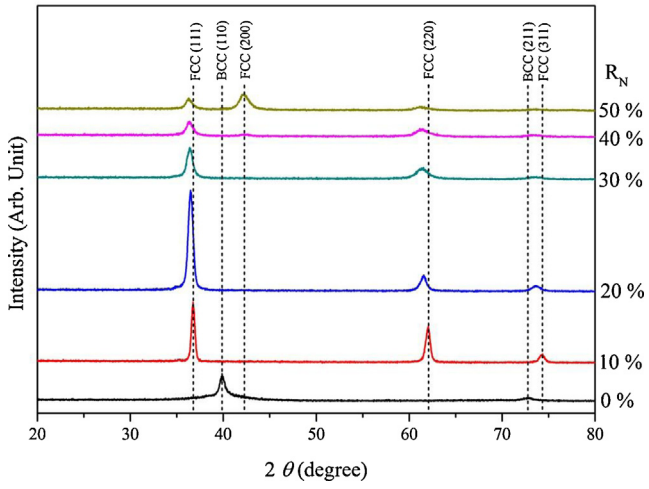

Fig. 3. X-ray diffraction pattern of the (AlCrMoTaTi)N coatings deposited at various R_N.

similar to the findings in previous studies [20,21]. The deposition rate reduction at higher R_N was due to the nitridation of the target surface and lower sputtering efficiency of nitrogen ions compared with that of Ar ions.

3.2. Crystal structure

Fig. 3 illustrates the X-ray diffraction (XRD) patterns of (AlCrMoTaTi)N coatings deposited at various R_N values. Based on the XRD analysis, the relative diffraction peak intensities, grain sizes, and lattice constants were determined and are listed in Table 1. For the AlCrMoTaTi alloy coatings, two diffraction peaks corresponding to the (1 1 0) and (2 1 1) lattice planes of a body-centered cubic (bcc) crystal structure were observed. The high mixing entropies of multi-principal systems can significantly lower free energy, thereby lowering the tendency of being ordered. Consequently, more stable random solid solutions form more easily than ordered phases. In our study, Cr, Ta, and Mo exhibited bcc crystal structures at room temperature. The bcc structure of Ti at 1150 K can be retained at room temperature by alloying it with a few elements, such as Nb or V [22]. Thus, considering the effect of high mixing entropy, a bcc solid solution structure was formed. However, AlCrMoTaTi alloys were mainly composed of 53% amorphous phase and 47% bcc solid solution phase, similar to the report by Tsai et al. [23]. The compositions of the amorphous and bcc phases in the alloy coatings were qualitatively analyzed using TEM energy dispersive spectroscopy. No detectable second phase or significant elemental segregation was observed (not shown). A coexistence of amorphous and bcc phases has not yet been reported in other HEA coating systems. Most high-entropy alloy coatings with larger atomic size difference are easier to form single amorphous structure in the as-deposited condition, such as AlCrTaTiZr, AlCrTiMoSi, AlCrTiNbY, TiVCrZrHf, and TiVCrZrY. Small (not sufficient) atomic size difference and the tendency of all five elements to form BCC should be the major factors to account for the BCC phase formation besides amorphous phase. In Zhang et al's work, the atomic size difference was defined by following equation [24]:

$$\text{Atomic size difference} = \sqrt[100]{\sum_{j=1}^{n} c_i \left(\frac{1-r_i}{\bar{r}}\right)^2}$$

where $\bar{r} = \sum_{i=1}^{n} c_i r_i$, c_i and r_i are the atomic percentage and atomic radius of the ith element. The numerical factor 100 was used to amplify the data for clarity. Based on above equation, the atomic size difference of AlCrMoTaTi, AlCrTaTiZr [10], AlCrTiMoSi [25], AlCrTiNbY [26], TiVCrZrHf [9], and TiVCrZrY [8] was estimated to be 5.50, 7.86, 8.68, 12.21, 9.70, and 13.43, respectively. Therefore, severe lattice distortion caused by large atomic size difference may lead to amorphous tendency.

(AlCrMoTaTi)N coatings formed a simple face-centered cubic (fcc) solid solution structure. Despite the differences in the crystal structures of binary nitrides, (AlCrMoTaTi)N coatings crystallized in an fcc structure, indicating that the fcc structure that resulted from the incorporation of the fcc-forming binary nitrides accommodates effectively non-fcc binary nitrides. This behavior is apparently consistent with other deposited nitride systems, such as TiAlN and CrAlN [27,28], which still present a single fcc structure up to approximately 60% Al to Ti or Cr mole ratio. Table 1 shows that the (1 1 0) peak position of AlCrMoTaTi alloy coatings or the (2 0 0) peak position of (AlCrMoTaTi)N coatings deposited at R_N = 50% approximates the average value of mixed Al, Cr, Mo, Ta, and Ti, or their nitrides. This finding not only indicates the formation of a simple solid solution with an fcc structure from all of the constituent nitrides, but also confirms the effect of

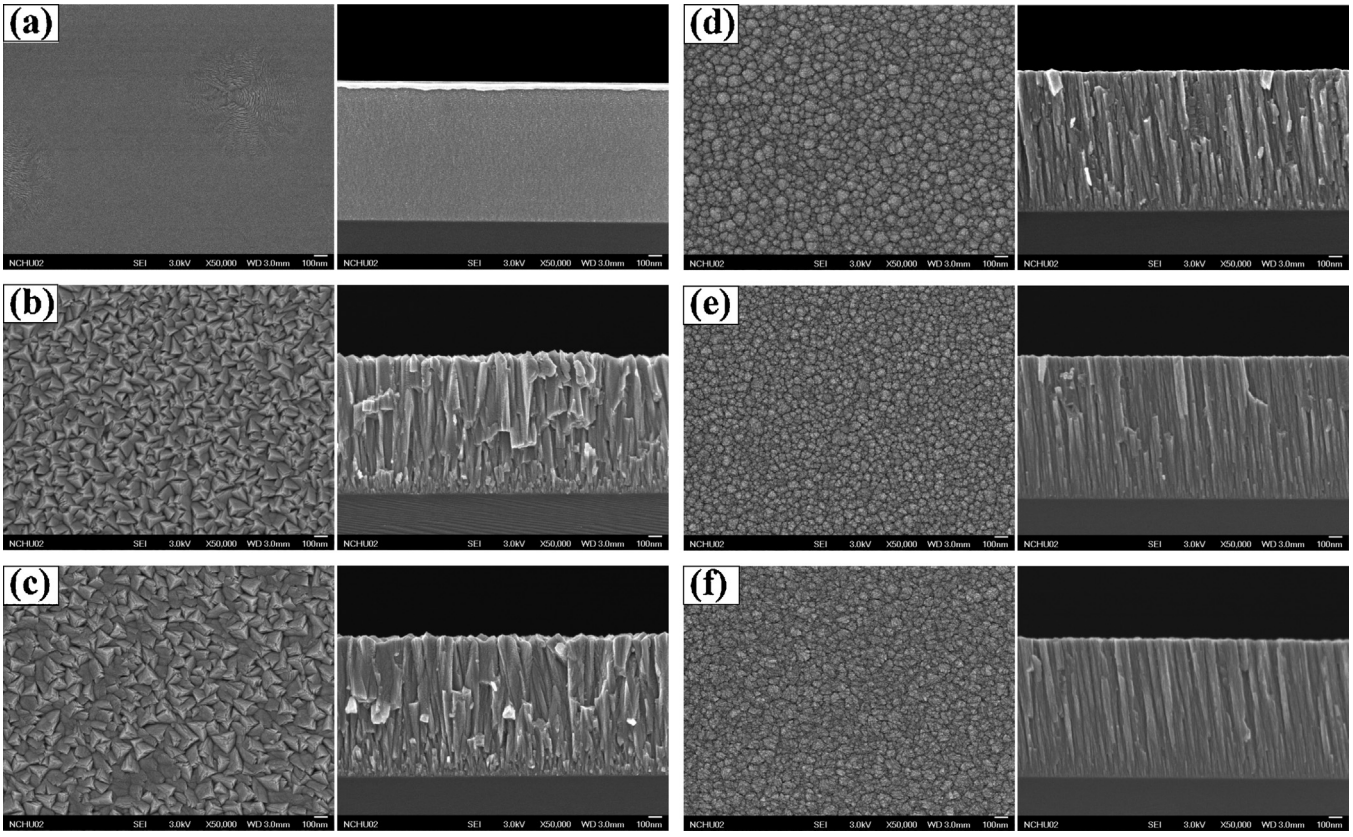

Fig. 4. SEM micrographs of the (AlCrMoTaTi)N coatings deposited at various R_N: (a) 0, (b) 10, (c) 20, (d) 30, (e) 40 and (f) 50%.

Table 1
Relative intensities of diffraction peaks, average crystallite sizes and lattice constant of (AlCrMoTaTi)N coatings.

R_N (%)	Relative intensity			Average crystallite size (nm)	Lattice constant (Å)
	(1 1 0)	(2 0 0)	(2 1 1)		
0	845.3	–	72.8	8.6	3.19245
R_N (%)	Relative intensity			Average crystallite size (nm)	Lattice constant (Å)
	(1 1 1)	(2 0 0)	(2 2 0)		
10	717.9	–	594.5	20.04	4.23196
20	1827.7	–	391.9	14.44	4.26212
30	710.6	–	489.8	9.87	4.27205
40	384.7	36.1	374.6	7.91	4.27512
50	276.2	541.7	154.0	7.86	4.28155

high entropies on simplifying crystal structures. Moreover, the lattice parameter increased from 0.4232 nm to 0.4282 nm when R_N increased because coatings deposited at higher R_N values have fewer vacant nitrogen sites. This phenomenon is similar to that discovered by Kang et al. for TiN alloys [29].

In terms of preferred orientation, AlCrMoTaTi alloys possessed a strong (1 1 0) bcc orientation with fewer (2 1 1) orientations. This characteristic was due to the fact that the (1 1 0) plane is the most densely packed among bcc crystal structures such that this plane has the lowest energy surface for a thin film to grow [30]. When R_N = 10%, some nitrides were expected to form, and the (AlCrMoTaTi)N coatings predominantly had a (1 1 1) fcc orientation with relatively minor ones. As R_N increased to 40% and 50%, the (2 0 0) peak emerged and was preferred to form. Such change in the preferred orientation with an increase in R_N was due to competitive growths. While there are initially equal distributions of (1 1 1) and (2 0 0) islands, the former orientation eventually dominates due to anisotropies in surface diffusivities. That is, the average adatom residence time is significantly higher at lattice sites on low diffusivity (1 1 1) surfaces versus high diffusivity (2 0 0) surfaces. Thus, adatoms which are stochastically deposited near grain boundaries and, through surface diffusion, sample sites on both sides of the boundary have a higher probability of becoming incorporated at the low-diffusivity surface which provides the more stable, lower potential energy sites. Thus, (1 1 1) grains with low surface diffusivities grow faster. Atomic shadowing exacerbates the difference, as protruding surfaces capture more off-normal flux. Thus, low-diffusivity (1 1 1) grains slowly expand and overgrow the high-diffusivity grains. In other words, a (1 1 1) orientation is preferred to form. However, when sputtering at enough high R_N, the change from (1 1 1) to (2 0 0) preferred orientation is observed. According to the report by Gall et al. [31], with increasing N_2 partial pressure or J_i/J_{Ti} flux ratio, the dissociation of N_2^+ species becomes more effective and provides a continuous source of atomic N, which, after chemisorption, can significantly alter the surface mobility of Ti adatoms depending on whether the surface is (0 0 1) or (1 1 1) oriented. Evidently, low-diffusivity surfaces change from (1 1 1) to the (2 0 0) planes, thereby resulting in a (2 0 0) preferred orientation growth [32,33,8]. Another reason describes this phenomena well. Generally, the preference of (2 0 0) orientation with lowest surface energy is understood in terms of adatom mobility during the growth. More specific, the transition is believed to occur at a critical ion-to-atom ratio, because the ion-to-atom ratio influences the adatom mobility during the growth in a positive way [32]. As such, the transition from the transition from (1 1 1) to (2 0 0) preferred orientation is believed to occur at a certain N_2 partial pressure, because the ion-to-atom ratio increases with increasing N_2 partial pressure [34].

R_N also has a strong effect on crystallinity and grain sizes, as listed in Table 1. When R_N increased from 10% to 20%, the (1 1 1) peak intensity increased sharply, indicating crystallinity improvement. However, grain sizes significantly decreased. For (AlCrMoTaTi)N coatings with $R_N \geq 30\%$, the peak intensity gradually decreased. Grain sizes further decreased with a considerable increase in R_N. As mentioned previously, fewer nitrogen site vacancies at higher R_N contribute to crystalline nitride formation. However, enhanced energy fluxes may cause a relatively larger resputtering effect. Thus, this effect at higher R_N significantly distorts the crystal lattice, thereby decreasing both crystallinity and grain sizes [35]. Subsequent AFM, SEM, and TEM characterizations were conducted to clarify further the structural evolution and observe the structural morphology of the coatings.

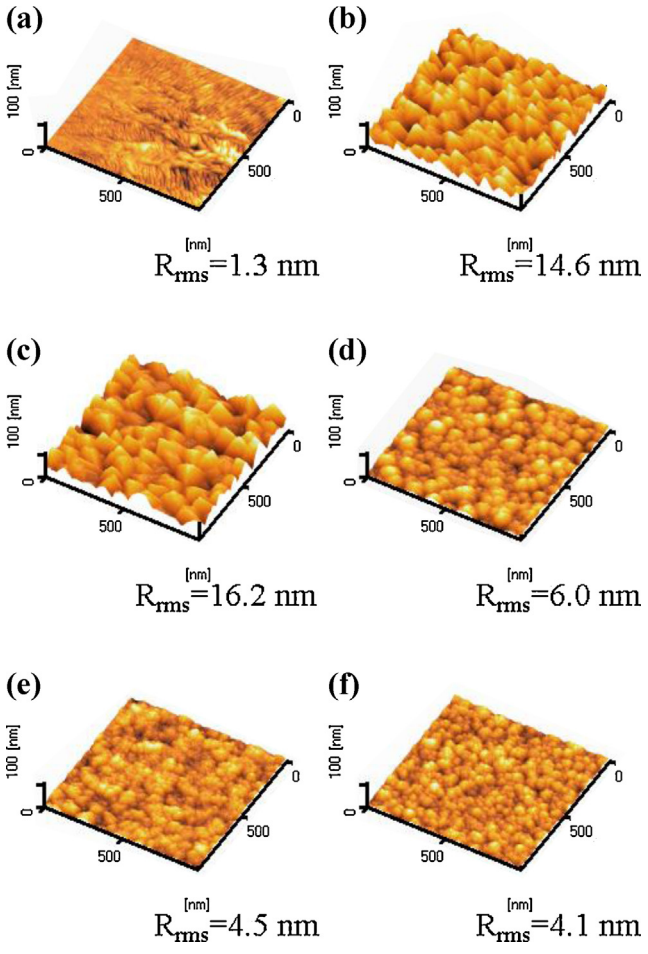

Fig. 5. AEM images of the (AlCrMoTaTi)N coatings deposited at various R_N: (a) 0, (b) 10, (c) 20, (d) 30, (e) 40 and (f) 50%.

3.3. Microstructure

Figs. 4 and 5 show the AFM and SEM images of the (AlCrMoTaTi)N coatings deposited at various R_N values, respectively. For AlCrMoTaTi alloy coatings, a dense structure with a slightly wrinkled surface and a small roughness of 1.3 nm was observed. Increasing R_N to 10% resulted in a V-shaped columnar structure with a clearly faceted surface and a large roughness of 14.6 nm. As R_N increased to 20%, the size of the columnar structure increased, and thus, roughness also rose to 16.2 nm. However, as R_N continued to increase to 50%, the surface morphology transformed to a dome-like structure along with a smaller columnar structure with a small roughness of 4.1 nm.

Figs. 6–8 demonstrate the TEM images with selected area diffraction (SAD) patterns of (AlCrMoTaTi)N coatings deposited at R_N = 0%, 20%, and 50%, respectively. Similar to the aforementioned SEM observations, no visible void existed in the AlCrMoTaTi alloy coatings. A closely packed equiaxed grain structure with different size distributions was observed (Fig. 6a and b). Based on the SAD patterns (Fig. 6c–e) with electron beams parallel to (1 0 0), (1 1 1), and (1 1 0), alloy coatings have an amorphous and bcc crystal structure. In general, the sputtered metal coatings usually develop

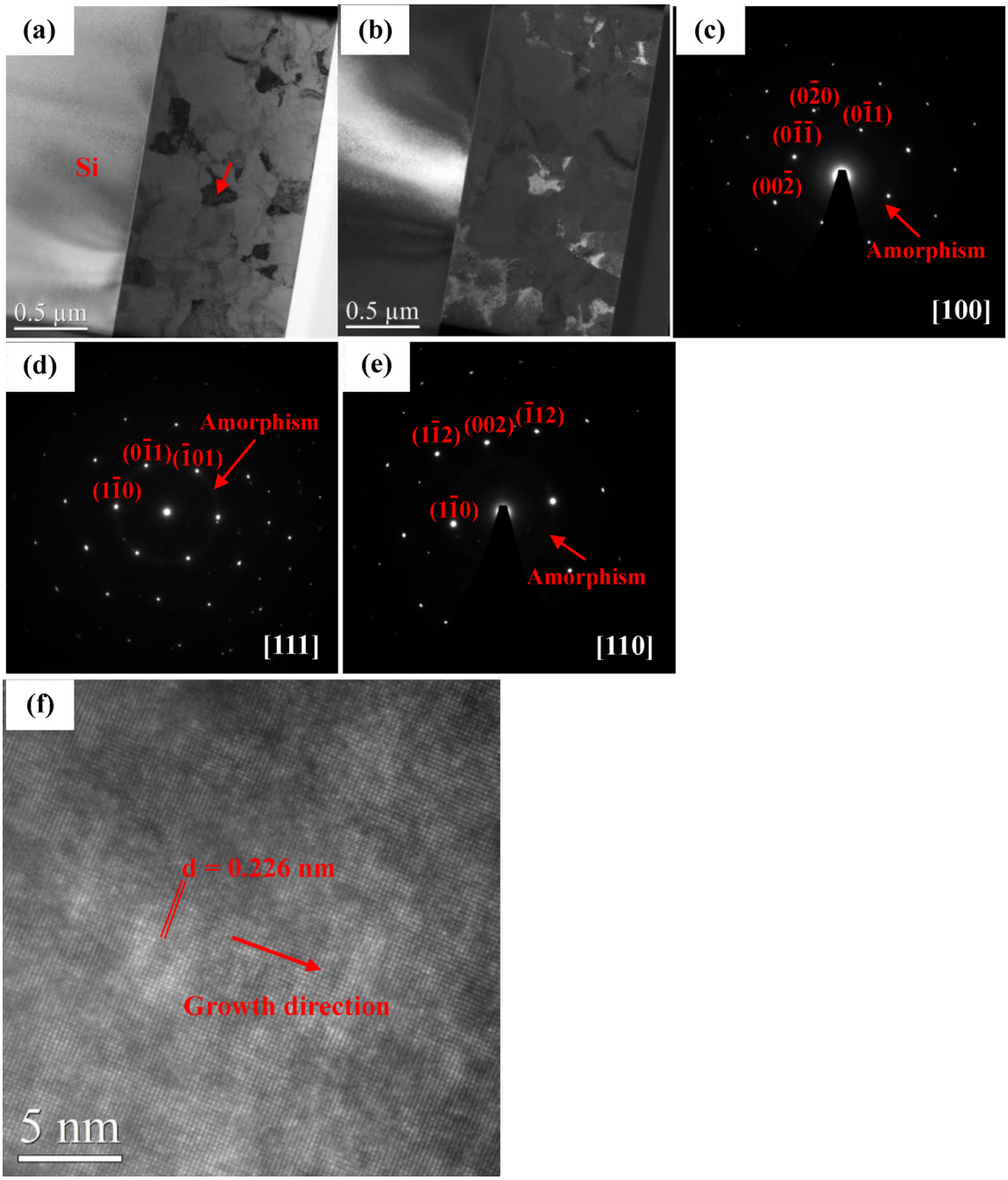

Fig. 6. Cross-sectional TEM micrographs of the AlCrMoTaTi alloy coating deposited at R_N = 0%. (a) Bright-field image. (b) Dark-field image using the (1 1 0) diffraction rings. (c–e) SAD patterns (indicated by the arrow) with the electron beam parallel to the directions of [1 0 0], [1 1 1], and [1 1 0]. (f) High resolution TEM lattice image (indicated by the arrow).

a columnar structure with crystal phase, mainly caused by self-shadowing. In this study, the coating growth significantly deviates from the columnar grain growth and forms an equiaxed grain structure with different size distributions. The energetic ion bombardment at high substrate bias can eliminate the shadowing effect and thus inhibit development of columnar structure. In addition, the incorporation of amorphous phase to the bcc phase can retard the columnar growth of bcc phase. As a reference, we determine the crystallographic orientation of a grain with its direction perpendicular to the substrate (out-of-plane orientation). Based on the high resolution TEM lattice image of a bcc crystal (Fig. 6f), the interplanar spacing along the growth direction is about 0.226 nm, concurrent with that of BCC (1 1 0). We denote the [1 1 0] axis direction to be parallel to the normal of the coating plane (the growth direction of the coating) and the [2 0 0] axis to lie in the plane misaligned by 45°, indicating that the [1 1 0] out-of-plane preferred orientation evolved.

When R_N was increased to 20%, the microstructure was transformed into V-shaped columns with pyramid-like and sharp-edged surface morphologies (Fig. 7a and b). Based on the SAD patterns and high resolution TEM lattice images, the out-of-plane preferred orientation of the underlayer changed from a random orientation at the bottom to a strong fcc (1 1 1) at the top (Fig. 7c and d). Grain sizes increased as the underlayer grew, resulting in a V-shaped columnar structure. This behavior is typical for evolutionary overgrowth mechanisms. During the early stages of growth, small grains with a

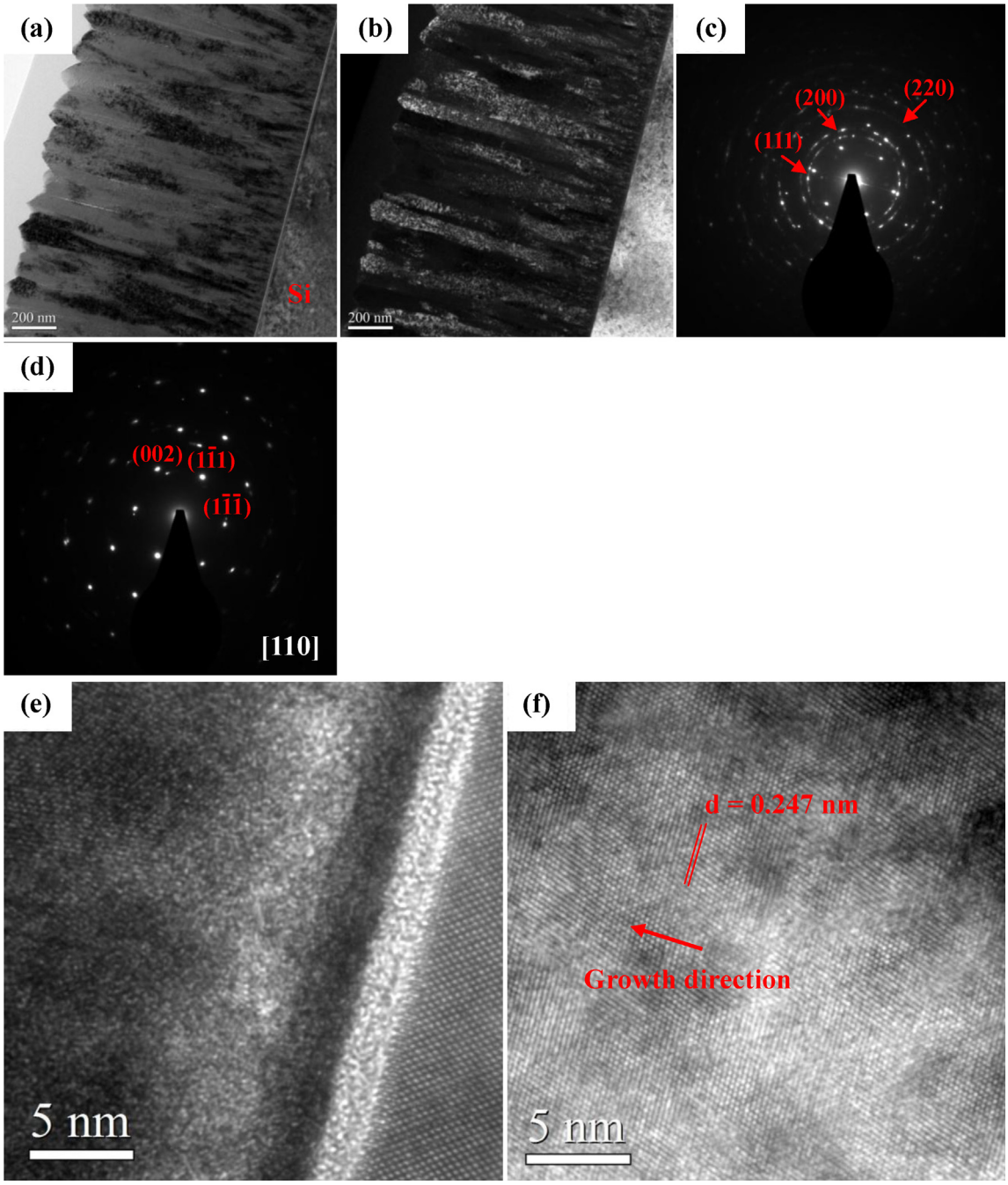

Fig. 7. Cross-sectional TEM micrographs of the (AlCrMoTaTi)N coating deposited at R_N = 20%. (a) Bright-field image. (b) Dark-field image using the (1 1 0) and (2 0 0) diffraction rings. (c) SAD patterns of bottom part of the cross-section. (d) SAD patterns of top part of the cross-section. (e) High resolution TEM lattice image of bottom part of the cross-section. (f) High resolution TEM lattice image of top part of the cross-section.

random orientation are formed on the substrate to reduce the surface energy (Fig. 7e). Adatoms that land on a (2 0 0)-oriented grain, having a high mobility, can reach the edge of that particular grain and contribute to lateral growth. However, if the (1 1 1)-oriented grains have low mobilities, perpendicular growth is induced. At coalescence, the (1 1 1)-oriented grains with the highest perpendicular growth speed overgrow the others (Fig. 7f). With this behavior, along with the shadowing effect, columnar structures with faceted tops and open column boundaries develop when the coating thickness increases. The interplanar distance along the growth direction is approximately 0.247 nm, which is equal to that of FCC (1 1 1).

As R_N continued to increase to 50%, evolutionary overgrowth was compressed (Fig. 8a and b), indicating that recrystallization and restructuring took place. Thus, the grains became non-faceted and [2 0 0] out-of-plane oriented (Fig. 8c–f), corresponding to the plane of the lowest surface energy. The interplanar distance along the growth direction is approximately 0.214 nm, which is equal to that of FCC (2 0 0). Moreover, considering a slight resputtering effect, the pores and voids in the coatings could be filled as much as possible, and consequently, an increase in the entire packed density of the coatings occurred. Simultaneously, grain refinement also occurred because of the increased renucleation rate of the growing coatings. This increase was induced by energetic bombardment-generated defects. The differences in the coating microstructure significantly contributed to the resulting coating properties.

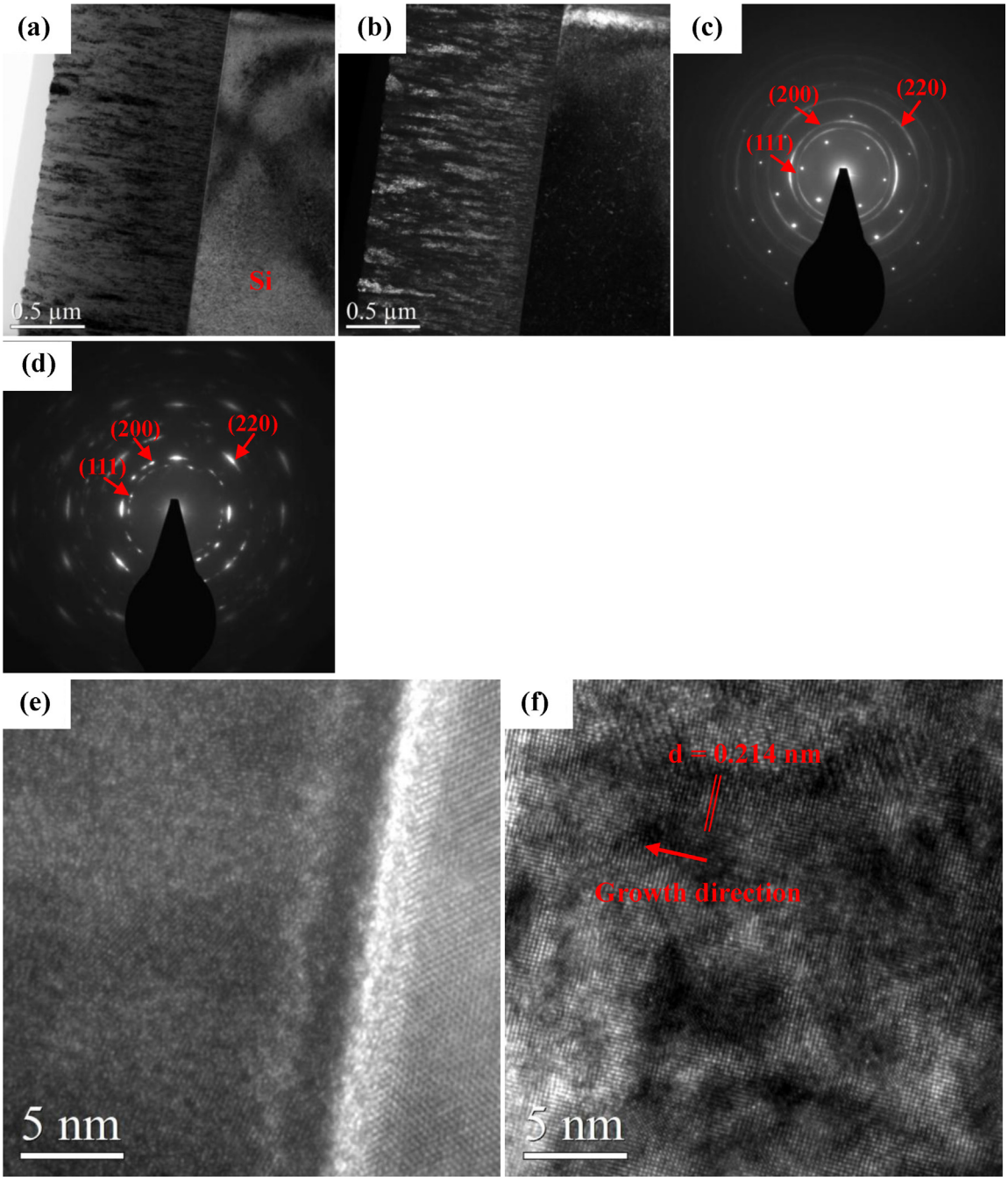

Fig. 8. Cross-sectional TEM micrographs of the (AlCrMoTaTi)N coating deposited at R_N = 50%. (a) Bright-field image. (b) Dark-field image using the (1 1 0) and (2 0 0) diffraction rings. (c) SAD patterns of bottom part of the cross-section. (d) SAD patterns of top part of the cross-section. (e) High resolution TEM lattice image of bottom part of the cross-section. (f) High resolution TEM lattice image of top part of the cross-section.

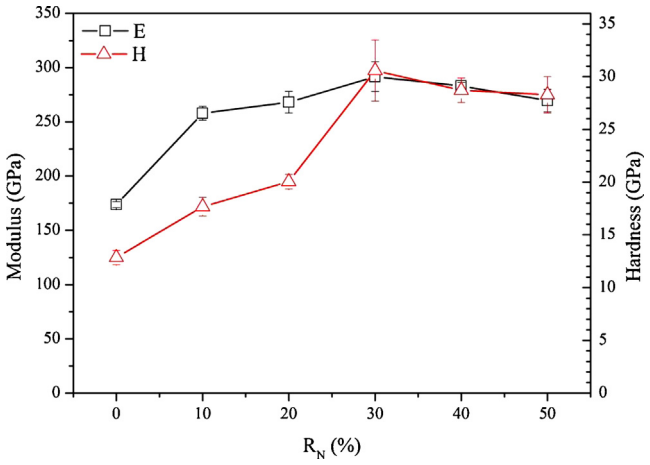

Fig. 9. Hardness and elastic modulus of the (AlCrMoTaTi)N coatings deposited at various R_N.

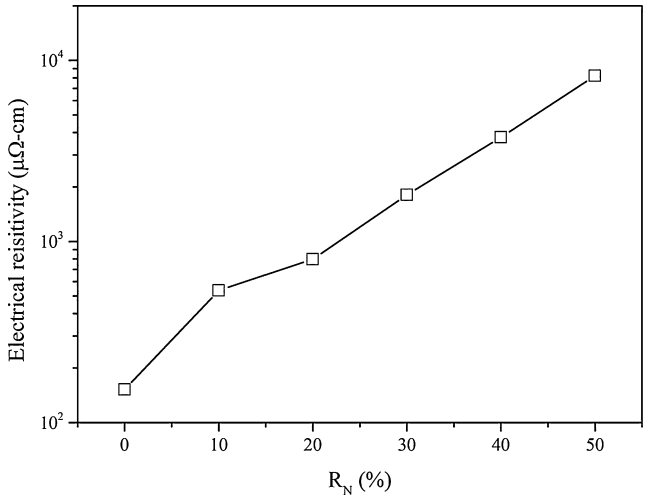

Fig. 10. Electrical resistivity of the (AlCrMoTaTi)N coatings deposited at various R_N.

3.4. Properties

Fig. 9 shows the elastic modulus and hardness of the (AlCrMoTaTi)N coatings deposited at various R_N values. For the AlCrMoTaTi alloy coatings, the elastic modulus and hardness values are 12.9 GPa and 173.7 GPa, respectively, which are relatively superior compared with typical coatings of pure metals and alloys. The high hardness is believed to be attributed to the considerable solid-solution strengthening effect caused by the addition of a large amount of different-sized atoms. At R_N = 10%, the hardness significantly increased to 20.6 GPa. This enhanced hardness was due to the strong Me–N bonding in the coating. When R_N increased to 30%, hardness reached a maximum value of 30.6 GPa. As R_N further increased, hardness remained almost constant at 28–29 GPa. Given this analysis, the preferred orientation, grain size, and densification of coatings significantly change as R_N increases. For fcc nitrides, the (1 1 1) orientations is generally the hardest orientation because of geometrical strengthening. The hardness of coatings is expected to increase as the (1 1 1) orientation increases. However, in this study, the coating hardness variation was not consistent with that of the (1 1 1) orientation. This result indicates that the preferred orientation of coatings does not account for the change in hardness with R_N. Strengthening of polycrystalline materials by grain size refinement is technologically attractive. The effect of smaller grain sizes on hardness is classically described by the Hall–Petch relationship. This relationship is based on dislocation pile-ups at grain boundaries. Intrinsic hardness could be approximated from bulk binary nitride hardness [36] using the mixture rule, obtaining a value of 13.3 GPa. Based on the analysis of (AlCrMoTaTi)N coatings deposited at R_N = 10% and 20%, grain size strengthening was calculated using the Hall–Petch equation. For the (AlCrMoTaTi)N coatings deposited at R_N = 30%, grain size strengthening was only approximately 10.0 GPa. However, their enhanced hardness reached 17.3 GPa, indicating that grain sizes are not the only dominant factor for the hardness of the present coatings. From the SEM and TEM observations, the microstructures were evidently converted from a columnar structure with void boundaries and a rough-faceted surface to a very dense structure with a smooth-domed surface. Therefore, coating densification is considered to be another dominant factor because the voids along the boundaries are eliminated when R_N increases from 20% to 30%. For the (AlCrMoTaTi)N coatings deposited at R_N = 40% and 50%, the effect of densification was negligible because no voids were detected along the boundaries. The slight decrease in hardness is inferred to originate from the reverse Hall–Petch effect, which has been reported for nanocrystalline materials with sufficiently small grain sizes (<10 nm) [37]. Plastic deformation in such a case is no longer dominated by dislocation motion, but by atomic sliding of grain boundaries.

Fig. 10 shows the electrical resistivity of the (AlCrMoTaTi)N coatings deposited at various R_N values. These alloy coatings have a lower electrical resistivity of 151.9 μΩ cm compared with nitride coatings because of the difference in nature of the bond characteristics. As R_N increased from 10% to 50%, electrical resistivity also increased from 536 μΩ cm to 8212 μΩ cm. Considering this increasing trend in electrical resistivity, the increased N content and reduced grain sizes (larger fraction of the grain boundary) are perceived to have the most effect in this study. According to the strong metal–non-metal bonding theory [38], metals provide charges to non-metals to form a metal–non-metal bonding. In this study, electrons were transferred from metal atoms to nitrogen atoms. Thus, the number of conduction electrons decreased, and electrical resistivity increased. The conductivity of the thin polycrystalline coatings strongly deviated from the conductivity of corresponding bulk single-crystalline materials because of the grain-boundary scattering effect. The grain boundary regions with disordered atom distributions resulted in severe electron scattering, thereby lowering the mobility rates of electrons.

4. Conclusion

(AlCrMoTaTi)N coatings were deposited at various R_N values via reactive RF magnetron sputtering. The N content increased rapidly at lower R_N values, and then reached around 50 at.% when R_N reached 50%. Composite equiaxed grain structures with amorphous and bcc crystal phases were observed in the alloy coatings. The composite structure is probably due to the reduced number of constituents with significant differences in their atomic size. The equiaxed grain structure is due to the combined contributions of energetic bombardment under bias conditions and two-phase composite structure. At R_N = 10% or 20%, nitride coatings exhibited a single fcc phase with a V-shaped columnar structure with faceted tops and open column boundaries, indicating an evolutionary growth mechanism. Significant decrease in grain sizes and increase in lattice parameter were observed with the increase in R_N. The microstructure was also converted to denser and smaller columns with a domed surface. The preferred orientation changed from (1 1 1) to (2 0 0), indicating that evolutionary overgrowth is compressed, and recrystallization and restructuring started to develop. The nitride coating hardness increased

from 17.7 GPa, reaching its maximum of 30.6 GPa at R_N = 30%. The corresponding dominant strengthening mechanism is attributed to coating densification and grain refinement. The slight softening at R_N = 40% was due to the inverse Hall–Petch effect in the ultrafine grain sizes. The significant increase in electrical resistivity of nitride coatings was mainly caused by grain-boundary scattering.

Acknowledgment

The authors gratefully acknowledge the financial support for this research by the National Science Council of Taiwan under grant no. NSC100-2221-E-005-034-MY3.

References

[1] H.O. Pierson, Handbook of Refractory Carbides and Nitrides, Noyes, New Jersey, 1996.
[2] M. Keunecke, C. Stein, K. Bewilogua, W. Koelker, D. Kassel, H. van den Berg, Surface and Coatings Technology 205 (2010) 1273–1278.
[3] L. Chen, Y. Du, S.Q. Wang, H.H. Xu, Materials Science and Engineering A 502 (2009) 671–675.
[4] Y.H. Cheng, T. Browne, B. Heckerman, E.I. Meletis, Surface and Coatings Technology 204 (2010) 2123–2129.
[5] C.K. Chung, H.C. Chang, S.C. Chang, M.W. Liao, Journal of Alloys and Compounds 537 (2012) 318–322.
[6] J.W. Yeh, S.K. Chen, S.J. Lin, J.Y. Gan, T.S. Chin, T.T. Shun, C.H. Tsai, S.Y. Chang, Advanced Engineering Materials 6 (2004) 299–303.
[7] P.K. Huang, J.W. Yeh, T.T. Shun, S.K. Chen, Advanced Engineering Materials 6 (2004) 74–78.
[8] D.C. Tsai, Y.L. Huang, S.R. Lin, S.C. Liang, F.S. Shieu, Applied Surface Science 257 (2010) 1361–1367.
[9] S.C. Liang, D.C. Tsai, Z.C. Chang, H.S. Sung, Y.C. Lin, Y.J. Yeh, M.J. Deng, F.S. Shieu, Applied Surface Science 258 (2011) 399–403.
[10] C.H. Lai, S.J. Lin, J.W. Yeh, S.Y. Chang, Surface and Coatings Technology 201 (2006) 3275–3280.
[11] D.C. Tsai, S.C. Liang, Z.C. Chang, T.N. Lin, M.H. Shiao, F.S. Shieu, Surface and Coatings Technology 207 (2012) 293–299.
[12] S.C. Liang, Z.C. Chang, D.C. Tsai, Y.C. Lin, H.S. Sung, M.J. Deng, F.S. Shieu, Applied Surface Science 257 (2011) 7709–7713.
[13] C.H. Lai, S.J. Lin, J.W. Yeh, A. Davison, Journal of Physics D 39 (2006) 4628–4633.
[14] M.H. Shiao, S.A. Kao, F.S. Shieu, Thin Solid Films 375 (2000) 163–167.
[15] S. Han, H.Y. Chen, Z.C. Chang, J.H. Lin, C.J. Yang, F.H. Lu, F.S. Shieu, H.C. Shih, Thin Solid Films 375 (2003) 163–167.
[16] X. Liua, G.J. Ma, G. Sun, Y.P. Duan, S.H. Liu, Applied Surface Science 258 (2011) 1033–1037.
[17] G. Gassner, P.H. Mayrhofer, K. Kutschej, C. Mitterer, M. Kathrein, Surface and Coatings Technology 201 (2006) 3335–3341.
[18] H.P. Klug, L.E. Alexander, X-ray Diffraction Procedures for Polycrystalline and Amorphous Materials, Wiley & Sons, New York, 1974.
[19] N. Laegreid, G.K. Wehner, Journal of Applied Physics 32 (1961) 365–369.
[20] L.F. Donaghey, L.G. Geraghty, Thin Solid Films 38 (1976) 271–280.
[21] M. Yoshitake, K. Takiguchi, Y. Suzuki, S. Ogawa, Journal of Vacuum Science and Technology A 6 (1988) 2326–2332.
[22] A.J. Maeland, G.G. Libowitz, J.F. Lynch, Journal of the Less Common Metals 104 (1984) 361–364.
[23] D.C. Tsai, Y.L. Huang, S.R. Lin, D.R. Jung, F.S. Shieu, Applied Surface Science 257 (2011) 3969–3973.
[24] Y. Zhang, Y.J. Zhou, J.P. Lin, G.L. Chen, P.K. Liaw, Advanced Engineering Materials 10 (2008) 534–538.
[25] H.W. Chang, P.K. Huang, A. Davison, J.W. Yeh, C.H. Tsau, C.C. Yang, Thin Solid Films 516 (2008) 6402–6408.
[26] M. Braic, V. Braic, M. Balaceanu, C.N. Zoita, A. Vladescu, E. Grigore, Surface and Coatings Technology 204 (2010) 2010–2014.
[27] M. Zhou, Y. Makino, M. Nose, K. Nogi, Thin Solid Films 339 (1999) 203–208.
[28] A. Kimura, M. Kawate, H. Hasegawa, T. Suzuki, Surface and Coatings Technology 169 (2003) 367–370.
[29] J.H. Kang, K.J. Kim, Journal of Applied Physics 86 (1999) 346.
[30] D.C. Tsai, Y.L. Huang, S.R. Lin, D.R. Jung, S.Y. Chang, F.S. Shieu, Journal of Alloys and Compounds 509 (2011) 3141–3147.
[31] D. Gall, S. Kodambaka, M.A. Wall, I. Petrov, J.E. Greene, Journal of Applied Physics 93 (2003) 9086–9094.
[32] J.E. Greene, J.-E. Sundgren, L. Hultman, I. Petrov, D.B. Bergstrom, Applied Physics Letters 67 (1995) 2928–2930.
[33] L. Hultman, E. Sundgren, J.E. Greene, D.B. Bergstrom, I. Petrov, Journal of Applied Physics 78 (1995) 5395–5403.
[34] S. Mahieu, P. Ghekiere, G. De Winter, R. De Gryse, D. Depla, G. Van Tendeloo, O.I. Lebedev, Surface and Coatings Technology 200 (2006) 2764–2768.
[35] P.K. Huang, J.W. Yeh, Surface and Coatings Technology 203 (2009) 1891–1896.
[36] A.W. Weimer, Carbide, Nitride and Boride Materials Synthesis and Processing, London, New York, 1997.
[37] R.W. Siegel, G.E. Fougere, Nanostructured Materials 6 (1995) 205.
[38] L.E. Toth, Transition Metal Carbides and Nitrides, Academic Press, New York NY, 1971.